

# Respiratory Signal Generation for Retrospective Gating of Cone-Beam CT Images

Stefan Wiesner<sup>a</sup>, Ziv Yaniv<sup>b</sup>

<sup>a</sup>Chair for Computer Aided Medical Procedures (CAMP), Technical University Munich

<sup>b</sup>Imaging Science and Information Systems (ISIS) Center, Dept. of Radiology,  
Georgetown University Medical Center, Washington, DC, USA

## ABSTRACT

We are currently investigating the acquisition of 4D cone-beam CT data using retrospective gating of the X-ray projection images. This approach requires a respiratory signal that is synchronized with image acquisition. To obtain such a signal we propose to use a spherical fiducial attached to the patient's skin surface such that it is visible in the images. A region of interest containing the fiducial is manually identified in an initial image and is then automatically detected in all other images. Subsequently, we perform an approximate spatial (3D) reconstruction of the marker location from its 2D locations. Finally, we compute a respiratory signal by projecting the 3D points onto the major axis estimated via principle component analysis. As this respiratory signal was obtained from the fiducial location in each of the images it is implicitly synchronized with image acquisition. We evaluate the robustness of our fiducial detection using an anthropomorphic respiratory phantom. To evaluate the quality of the estimated respiratory signal we use a motion platform that follows the respiratory motion obtained by tracking the skin surface of a volunteer. We show that our method generates a respiratory signal that is in phase with the ground truth signal, but suffers from inaccuracies in amplitude close to the anterior-posterior imaging setup where the primary direction of motion is perpendicular to the image plane. Thus, our method should only be used for phase based retrospective gating.

**Keywords:** image-guided therapy, respiratory motion, respiratory signal, cone-beam CT, trajectory reconstruction

## 1. INTRODUCTION

The use of image-guided navigation systems has grown in popularity in the past decade, as they typically enable procedures that involve substantially less trauma for the patient. To date, these systems have primarily been applied in procedures that involve rigid or semi-rigid structures such as those encountered in neurosurgery and orthopedics.<sup>1</sup> More recently researchers have turned their attention to interventions involving anatomical structures that move and deform due to respiration. Two key components have been identified as enabling technologies for such procedures, motion modeling and intra-operative imaging.<sup>2</sup>

Currently, image-guided interventions performed in the thoracic-abdominal region use a gated approach. That is, a single three dimensional CT volume is acquired at breath-hold and the physician advances only during the respiratory phase in which the image was acquired.<sup>3</sup> This has the undesirable effect of increasing the procedure time. To enable a more streamlined workflow we propose to use a 4D, 3D over time, Cone-Beam CT (CBCT) data set. In this manner, we can provide a dynamic image display throughout the respiratory cycle.

Our 4D CBCT acquisition approach is based on retrospective binning, similar to that used in 4D CT reconstruction.<sup>4</sup> The X-ray projection images are binned according to their phase in the respiratory cycle, and 3D reconstruction is performed separately for each bin. A prerequisite of this approach is that we have a respiratory signal that is synchronized with image acquisition.

A variety of devices exist for generating a respiratory signal. These include, devices based on the temperature of airflow,<sup>5</sup> on direct measurement of airflow,<sup>6</sup> on the tension of a belt placed on the patient,<sup>7</sup> and on tracking

---

E-mail: zivy@isis.georgetown.edu

skin surface motion. The later are either monocular camera systems using infrared<sup>8,9</sup> or standard video<sup>10</sup> images, and stereo camera systems, again, using infrared<sup>11</sup> or standard video.<sup>12</sup>

In our context, 4D CBCT reconstruction, these systems have two main drawbacks. They introduce additional hardware that is currently not part of the acquisition protocol, and they require synchronization with the image acquisition. An alternative approach proposed by several authors is to generate a respiratory signal directly from the projection images.<sup>13-15</sup> This approach has the added advantage of not requiring additional hardware, and more importantly it is implicitly synchronized with image acquisition.

In<sup>15</sup> the respiratory signal is generated by tracking features in the X-ray projection images. The tracked features are limited to the region of the diaphragm, as this region exhibits the maximal motion due to respiration. The 2D feature locations are projected onto the superior-inferior axis and those with maximal motion are used to generate the respiratory signal based on their displacement along the superior-inferior direction.

In<sup>14</sup> this work was extended. In this case, features are sampled uniformly across the region of the lungs. They are then tracked in the 2D images. Features that are only visible for a short period of time or move only slightly are discarded. For all other features, the 2D locations of each feature are projected onto the least squares line fit to them. This yields a respiratory signal from a single feature. All signals are combined by linearly normalizing their magnitude to be in  $[0, 1]$  and taking the mean value for each point in time. The authors note that most of the feature points retained by their approach are in the region of the diaphragm and are thus in agreement with the previous approach,<sup>15</sup> although some features are located on the lung walls.

In<sup>13</sup> a  $1mm$  radio-opaque fiducial is placed on the patients skin and is tracked in the X-ray projection images. The 2D fiducial locations are projected onto the superior-inferior axis and this is the 1D respiratory signal. The primary difference between this approach and the previous two<sup>14,15</sup> is that those approaches track regions of interest that do not correspond to a consistent spatial anatomical structure, as both the X-ray source and anatomy are moving, and this approach does track a specific spatial point.

Non of these approaches presents an explicit spatial motion model, rather, they empirically show that their approach is either correlated with a known respiratory signal or that it can be used for 4D CBCT reconstruction. In this paper we present an explicit spatial motion model, taking into account the anatomical and X-ray source motions. This model is then used to derive a respiratory signal based on the motion of a skin fiducial that is visible in the projection images.

## 2. MATERIALS AND METHODS

The CBCT system used in our work is the Axiom Artis dFA system (Siemens AG, Medical Solutions, Erlangen, Germany). This is a floor mounted C-arm CBCT system based on a solid-state flat panel detector. Projection images are acquired using a 20sec rotation in which 543 images are uniformly acquired over a rotation of  $220^\circ$ . Image dimensions are  $960 \times 1024$  pixels. The system is modelled as a distortion-less pinhole camera as this has been shown to be an appropriate approximation of the imaging process.<sup>16</sup> The skin adhesive fiducials used in this work are the 4mm spherical CT-SPOTS markers (Beekley Corp., Bristol CT, USA).

To obtain a respiratory signal that is implicitly synchronized with image acquisition we estimate the approximate spatial (3D) location of a skin adhesive radio-opaque fiducial throughout the data acquisition process. The fiducial is localized in each of the 2D CBCT projection images and its 3D location is estimated using a linear approximation of its spatial trajectory. Once the 3D fiducial locations are obtained we perform Principle Component Analysis (PCA), and project the points onto the major axis. This is our one dimensional respiratory signal. As the signal is based on the 3D fiducial locations which are tied to specific 2D projection images it is implicitly synchronized with the image acquisition.

We next describe our approach in detail.

### 2.1 Fiducial localization

Fiducial localization is performed automatically, following manual initialization. In the first image the user indicates a rectangular region of interest containing the fiducial. For each image we perform edge detection in the region of interest using the Canny edge detector.<sup>17</sup> The edge detector's high and low thresholds are set to

0.5 and 0.2 (pixel values are in  $[0, 1]$ ) and the smoothing parameter  $\sigma$  is set to 1.0. On the resulting edge image we perform circle estimation using the Random Sample Consensus (RANSAC) algorithm.<sup>18</sup>

RANSAC is an algorithm for dealing with outliers in a parameter estimation problem. Instead of using the whole data set to compute a least squares estimate of the model's parameters, minimal subsets are randomly selected, and the model parameters are estimated for each subset. For each model a consensus set is obtained by measuring the distance of each point to the solution and incorporating it into the set if it is below a user specified threshold. The process is repeated until the model with the largest support has been found. This consensus set is then used to compute a least squares estimate of the model parameters. In our case, circle fitting, the minimal subset size is three and the circle is parameterized by its center coordinates and radius.

To utilize the RANSAC algorithm we thus need to define the following: 1) a method for parameter estimation with the minimal number of points; 2) a method for least squares parameter estimation; 3) a distance function; and 4) a function to check for degenerate point configurations.

In our case, estimation of the parameters of a circle, we use the same method to estimate the parameters from the minimal number of points and to compute a least squares estimate. We follow the derivation described in.<sup>19</sup> The nonlinear parametric circle equation is linearized and the circle parameters are extracted from the solution to this modified problem as follows. The circle equation is written as:

$$a\mathbf{x}^T\mathbf{x} + \mathbf{b}^T\mathbf{x} + c = 0 \quad (1)$$

yielding the following linear equation system

$$\begin{pmatrix} x_{11}^2 + x_{12}^2 & x_{11} & x_{12} & 1 \\ x_{21}^2 + x_{22}^2 & x_{21} & x_{22} & 1 \\ & \vdots & & \\ x_{n1}^2 + x_{n2}^2 & x_{n1} & x_{n2} & 1 \end{pmatrix} \begin{pmatrix} a \\ b_1 \\ b_2 \\ c \end{pmatrix} = 0 \quad (2)$$

which has an exact solution for three non-collinear points and has a non-trivial least squares solution subject to the constraint  $\|(a, b_1, b_2, c)\| = 1$ . The circle center and radius are then obtained as

$$\mathbf{x}_{center} = \left(-\frac{b_1}{2a}, -\frac{b_2}{2a}\right) \quad r = \sqrt{\frac{\|b\|^2}{4a^2} - \frac{c}{a}} \quad (3)$$

This assumes that  $a \neq 0$  which in our case is valid, as otherwise the equation would describe a line ( $\mathbf{b}^T\mathbf{x} + c = 0$ ).

Our distance function describes the distance between a point,  $\mathbf{x}$ , and a circle model,  $(\mathbf{x}_{center}, r)$  and is

$$d = \left| \|\mathbf{x}_{center} - \mathbf{x}\| - r \right| \quad (4)$$

Finally, to ensure that we do not attempt to estimate circle parameters from degenerate subsets, three collinear points, we evaluate how close the sample set points are to a linear configuration. This is done by computing the eigen-values of the covariance matrix of the sample set. If the largest eigen-value is an order of magnitude larger than the second largest one, the sample set is discarded, as it is too close to a line.

Once the maximal consensus set is obtained we fit a circle to it, with the circle center being the fiducial location that we desire. We then shift the region of interest in the following image so that it is centered on the previously detected circle center and repeat the process. The distance between 2D fiducial locations in two consecutive images is small due to the speed of image acquisition, 0.036sec between image acquisitions with a  $0.4^\circ$  C-arm rotation, allowing us to use a small region of interest for fiducial tracking.

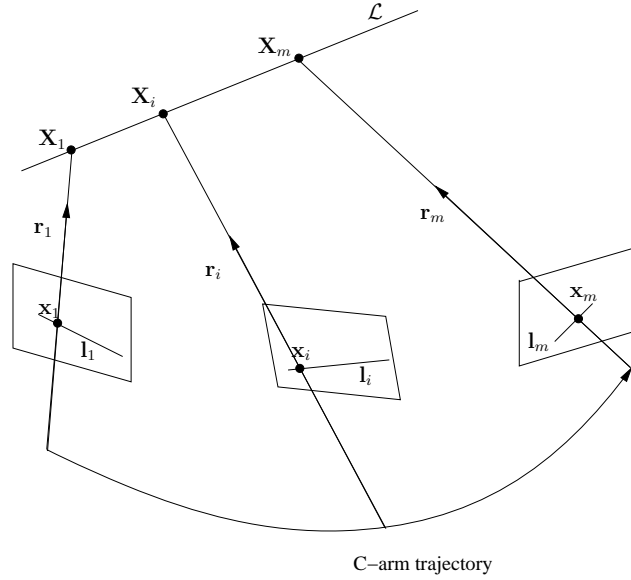


Figure 1. Trajectory triangulation of a linear trajectory. The line  $\mathcal{L}$  is estimated from the known camera parameters and motion, and the 2D point locations. The 3D point locations are then estimated as the intersection points of the rays  $\{\mathbf{r}\}_i$  and the line  $\mathcal{L}$ .

## 2.2 Spatial location estimation

Our goal is to estimate the fiducial's 3D location at the time of image acquisition, based on its 2D location in the image and the known camera motion and parameters. A similar problem was studied in the field of computer vision.<sup>20</sup> In that context, the point of interest was constrained to move along linear or conic shaped trajectories. The 3D point locations were estimated in two steps. First the trajectory was estimated and then the spatial location corresponding to each of the images was estimated as the intersection of the trajectory and the ray emanating from the camera location and going through the image point corresponding to the 2D point location. Hence, the approach was coined "trajectory triangulation". Figure 1 illustrates this concept.

In our case the fiducial trajectory is not linear, but is close enough so that a linear approximation of the motion is reasonable. This is based on our empirical observations which we qualitatively confirmed using data acquired from a volunteer, as described in section 3. We next describe the analytic trajectory estimation method due to Avidan and Shashua,<sup>20</sup> and explain why it fails in our case, followed by our iterative non-linear method for trajectory estimation.

### 2.2.1 Analytic trajectory estimation

We now derive the analytic estimation method for a linear trajectory due to Avidan and Shashua<sup>20</sup> and explain why, in our case, it is less accurate than our nonlinear approach.

As our imaging apparatus is modelled as a projective camera we have

$$\mathbf{x}_i^T \mathbf{l}_i = 0 \quad (5)$$

where  $\mathbf{x}_i$  is the projection of  $\mathbf{X}_i$ , a point on the line  $\mathcal{L}$ , and  $\mathbf{l}_i$  is the projection of  $\mathcal{L}$  in a specific image. That is, equation 5 reflects the fact that incidence is invariant under projective transformations.

We now seek a way to relate the 3D line  $\mathcal{L}$  to its projections  $\mathbf{l}_i$  in the images.

A 3D line can be represented by two points,  $\mathbf{p}, \mathbf{q}$ , on it. Using homogenous points,  $[\mathbf{p}, 1], [\mathbf{q}, 1]$  the line,  $\mathcal{L}$ , is described in Plücker coordinates as:

$$\mathbf{L} = [\mathbf{p} \times \mathbf{q}, \mathbf{q} - \mathbf{p}] \quad (6)$$

Note that the Plücker coordinate vector  $\mathbf{L}$  corresponds to a 3D line only if it satisfies the following two constraints:

$$\begin{aligned} \mathbf{L}_1\mathbf{L}_4 + \mathbf{L}_2\mathbf{L}_5 + \mathbf{L}_3\mathbf{L}_6 &= 0 \\ \neg(\mathbf{L}_4 = 0 \wedge \mathbf{L}_5 = 0 \wedge \mathbf{L}_6 = 0) \end{aligned} \quad (7)$$

To project the 3D homogenous line representation onto the image we reformulate the projection matrix  $P$ . Note that  $P$  encodes both the external and internal camera parameters. The  $3 \times 4$  matrix  $P$  becomes a  $3 \times 6$  line projection matrix  $\tilde{P}$ .<sup>21</sup>

$$\tilde{P} = [\det(\bar{P})\bar{P}^{-T} \ [P_{1..3,4}]_{\times}\bar{P}]; \quad (8)$$

where:

$$\bar{P} = P_{1..3,1..3}$$

and

$$[P_{1..3,4}]_{\times} = \begin{bmatrix} 0 & -P_{3,4} & P_{2,4} \\ P_{3,4} & 0 & -P_{1,4} \\ -P_{2,4} & P_{1,4} & 0 \end{bmatrix}$$

Substituting the line representation, Equation 6, and the line projection matrix, Equation 8, into Equation 5 yields the following equation system:

$$\mathbf{x}_i^T \tilde{P}_i \mathbf{L} = 0; \quad (9)$$

whose solution yields the desired line,  $\mathbf{L}$ . For a unique solution to exist five or more images are required.

While this method is elegant it has one flaw, the constraints on the solution (Equation 7) are not explicitly enforced. That is, Equation 9 admits solutions that do not correspond to a 3D line. Given this flaw, and our data, which is only approximately linear this method was found to be less accurate than our nonlinear approach.

## 2.2.2 Non-linear trajectory estimation

We now derive our geometry-based nonlinear trajectory estimation method. We represent the directional line,  $\mathcal{L}$  as  $[\mathbf{p}, \mathbf{n}]$ , where  $\mathbf{p}$  is a 3D point on the line and  $\mathbf{n}$  is the line's 3D direction.

We formulate the linear trajectory estimation task as a non-linear optimization problem by observing that the linear trajectory we seek minimizes the distance from all back-projected rays,  $\mathbf{r}_i = [\mathbf{q}_i, \mathbf{v}_i]$ , defined by the camera and projected fiducial pairs:

$$[\mathbf{p}^*, \mathbf{n}^*] = \arg \min_{\mathbf{p}, \mathbf{n}} \sum_i d(\mathbf{p}, \mathbf{n}, \mathbf{q}_i, \mathbf{v}_i) \quad (10)$$

We start by computing the backprojected rays from the pairs of projection matrices and image points. The point on the ray,  $\mathbf{q}$ , and the ray direction,  $\mathbf{v}$ , are computed from the projection matrix and fiducial projection as:

$$\begin{aligned} \mathbf{q} &= -P_{3 \times 3}^{-1} P_4 \\ \mathbf{v} &= P_{3 \times 3} \mathbf{x} \end{aligned}$$

with  $\mathbf{q}$  being the camera origin,  $P_{3 \times 3}$  the upper left  $3 \times 3$  sub-matrix of the projection matrix  $P$ ,  $P_4$  its last column and  $\mathbf{x}$  the homogenous image point.<sup>22</sup>

The distance between two skew lines  $[\mathbf{p}, \mathbf{n}]$  and  $[\mathbf{q}, \mathbf{v}]$  as utilized in Equation 10 is given by:

$$d = \|\mathbf{y} - \mathbf{z}\| \quad (11)$$

where  $\mathbf{y}$  and  $\mathbf{z}$  are the closest points on each line,

$$\mathbf{y} = \mathbf{p} + \frac{[(\mathbf{q} - \mathbf{p}) \times \mathbf{v}] \cdot \mathbf{w}}{\mathbf{w} \cdot \mathbf{w}} \mathbf{n} \quad \mathbf{z} = \mathbf{q} + \frac{[(\mathbf{q} - \mathbf{p}) \times \mathbf{n}] \cdot \mathbf{w}}{\mathbf{w} \cdot \mathbf{w}} \mathbf{v} \quad (12)$$

and

$$\mathbf{w} = \mathbf{n} \times \mathbf{v} \quad (13)$$

The linear trajectory is then obtained by minimizing Equation 10.

As our method uses nonlinear optimization it requires initialization. The line direction,  $\mathbf{n}^*$ , is initialized as  $[0, 1, 0]$ . This is based on our knowledge of the imaging apparatus coordinate system and assumes that the patient is in the supine position. The point on the line,  $\mathbf{p}^*$  is initialized as the point that minimizes the sum of squared distances from all  $m$  backprojected rays:

$$\mathbf{p}^* = \arg \min_{\mathbf{p}} \sum_i \|(\mathbf{p} - \mathbf{q}_i) - \mathbf{v}_i^T (\mathbf{p} - \mathbf{q}_i) \mathbf{v}_i\|^2 \quad (14)$$

The above minimization is solved in an analytic manner by differentiating for  $\mathbf{p}$  and equating to zero, to obtain the following linear equation system whose solution is the point we seek:

$$\begin{pmatrix} m - \sum v_x^2 & -\sum v_x v_y & -\sum v_x v_z \\ -\sum v_x v_y & m - \sum v_y^2 & -\sum v_y v_z \\ -\sum v_x v_z & -\sum v_y v_z & -m - \sum v_z^2 \end{pmatrix} \mathbf{p} = \sum_{i=1}^m (\mathbf{q}_i - \mathbf{v}_i^T \mathbf{q}_i \mathbf{v}_i) \quad (15)$$

### 2.3 Respiratory signal generation

Given the linear trajectory,  $\mathcal{L}$ , we can estimate the 3D fiducial location using the backprojected ray for each image. In general the ray and line are skew. We estimate the 3D fiducial location as the point on the backprojected ray that is closest to the line  $\mathcal{L}$  (see equation 12). This is motivated by the fact that we know our point is on the backprojected ray, and that the trajectory is an approximation.

Once the 3D fiducial locations are obtained we perform Principle Component Analysis (PCA), and project the points onto the major axis. This is our one dimensional respiratory signal. Table 1 summarizes our framework for respiratory signal generation.

## 3. EXPERIMENTAL RESULTS

We experimentally evaluated our approach as follows. We first evaluated the validity of our linear trajectory approximation, and the effect of fiducial placement using data acquired from a volunteer. Then we evaluated the quality of our fiducial localization in projective X-ray images using an anthropomorphic respiratory phantom. We then evaluated the trajectory estimation methods using simulated data. Finally, we evaluated the whole approach using a computer controlled motion platform replicating the respiratory motion of a volunteer.

### 3.1 Linear trajectory and fiducial placement evaluation

To assess the validity of our linear trajectory approximation and the effect of fiducial placement on the respiratory signal we acquired surface motion data at seven locations on the thorax and abdomen of a volunteer using the Optotrak Certus (Northern Digital Inc., Waterloo, Ontario, Canada) tracking system. Data was acquired at a rate of  $60Hz$  with the volunteer in the supine position.

The surface motion was analyzed using Principle Component Analysis, with the results indicating that there is a single dominant direction of motion. Table 2 summarizes this experiment.

We then generated a respiratory signal from each of the seven 3D data sets by projecting the data onto the principle axis. Each of these respiratory signals was compared to all others using normalized cross correlation, Pearsons  $r$ . All signals were found to be correlated with a correlation coefficient above 0.99. Table 3 summarizes this evaluation.

1. Fiducial tracking (2D)
  - (a) Manually define a rectangular ROI in first frame.
  - (b) Perform edge detection in the ROI.
  - (c) Fit a circle to the edge data using the RANSAC algorithm.
  - (d) Shift ROI to circle center and repeat with next frame.
2. Trajectory estimation (3D)
  - (a) For each image compute the back-projected ray emanating from the X-ray source and going through the fiducial location
  - (b) Estimate the line that minimizes the distance to all back-projected rays.
3. Respiratory signal generation (1D)
  - (a) For each back-projected ray compute the 3D point on the ray that is closest to the estimated trajectory.
  - (b) Project the 3D point locations onto the principle axis, computed using PCA. This is the respiratory signal.

Table 1. Trajectory based framework for respiratory signal generation.

Marker	1	2	3	4	5	6	7	mean
eig X	1.42	1.42	1.16	1.45	1.52	1.23	1.18	1.34
eig Y	6.19	7.72	5.5	5.01	3.87	4.77	4.48	5.37
eig Z	77.08	81.14	70.29	66.79	48.12	69.18	53.33	66.56

Table 2. Eigenvalues corresponding to magnitude of motion, obtained via PCA.

Marker	1	2	3	4	5	6	7
1	1.0000	0.9999	0.9994	0.9996	0.9982	0.9991	0.9968
2		1.0000	0.9995	0.9996	0.9981	0.9992	0.9969
3			1.0000	0.9992	0.9990	0.9995	0.9985
4				1.0000	0.9986	0.9995	0.9976
5					1.0000	0.9992	0.9991
6						1.0000	0.9989
7							1.0000

Table 3. Correlation of respiratory signals computed from motion data of optotrak markers placed on the thorax and abdomen of a volunteer.

### 3.2 Fiducial localization evaluation

To evaluate the robustness of our fiducial detection we used an anthropomorphic respiratory phantom.<sup>23</sup> The spherical fiducial was attached to the phantom's thorax and X-ray images were acquired while the phantom was respiring. The fiducial detection algorithm was run and resulted in successful detections in all data sets, as judged by visual inspection.

Figure 2 shows the experimental setup and sample images. One sees that even when only part of the fiducial contour is detected, due to overlap with the phantom's rib cage, the RANSAC based estimation yields a correct localization.

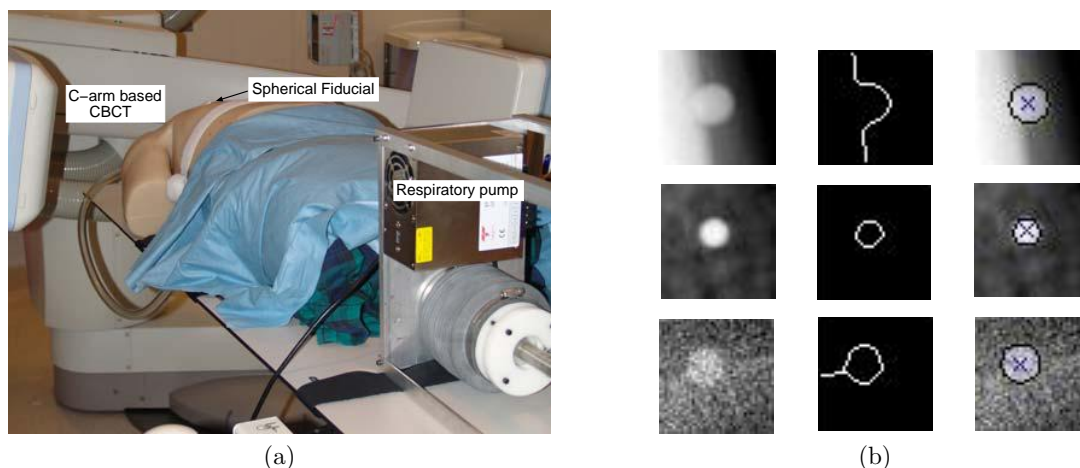


Figure 2. Fiducial localization (a) experimental setup; and (b) sample results from three C-arm poses, original image, detected edges, and estimated circle overlaid.

### 3.3 Trajectory estimation evaluation

To evaluate the trajectory estimation we performed three simulation studies. In all studies we utilized 3D points which were placed inside the known viewing volume of our CBCT system. We then projected these points using the actual camera projection matrices obtained from our system.

In the first study we randomly created 100 linear segments inside the viewing volume of the CBCT system with an angle of up to  $45^\circ$  from the  $y$  axis. We then generated 3D points by sampling along each segment using sinusoidal modulation. The sampled points were then projected using the CBCT projection matrices, and given as input to the trajectory estimation algorithms. This allowed us to assess the sensitivity of the two trajectory estimation methods to the trajectory direction.

To evaluate the quality of the trajectory estimation we use the angle between the known and estimated line directions, and the mean distance between the known 3D points and the estimated line. Table 4 summarizes this study. It can be seen that under optimal conditions without any noise the analytic method outperforms our nonlinear approach.

Method	Angular Error [degrees] ( $\mu$ , $\sigma$ , median, max)	Distance Error [mm] ( $\mu$ , $\sigma$ , median, max)
Analytic	(0.00, 0.00, 0.00, 0.00)	(0.00, 0.00, 0.00, 0.00)
Nonlinear	(1.17, 5.90, 0.00, 39.38)	(0.03, 0.16, 0.00, 1.56)

Table 4. Results of trajectory estimation for 100 randomly generated linear trajectories.

In the second study we arbitrarily chose a line, [ $\mathbf{p} = (0, 0, 0)$ ,  $\mathbf{n} = (0.0, 0.7, 0.7)$ ], inside the viewing volume of the CBCT system. We then generated 3D points and projected them as done in the previous study. Finally, noise ( $\sim N(0, 0.5)$ ) was added to the 2D coordinates, and this was the input to the two algorithms. The noise

generation and trajectory estimation steps were repeated 100 times for the given line. Evaluation was performed in the same manner as described above. Table 5 summarizes this study.

When dealing with directional data, the line direction, we can assess variability using the norm of the mean vector. This norm is in  $[0, 1]$ , with a smaller norm indicating more variability in the results. The mean of the estimated directions for the nonlinear method is  $[0.00, 0.70, 0.71]$ , norm 1.00, and for the analytic method  $[-0.04, 0.64, 0.48]$ , norm 0.80. As the norm of the mean vector for the nonlinear method is larger than that of the analytic method we conclude that it is more stable when presented with data with additive Gaussian noise.

Method	Angular Error [degrees] ( $\mu$ , $\sigma$ , median, max)	Distance Error [mm] ( $\mu$ , $\sigma$ , median, max)
Analytic	(30.57, 23.18, 21.34, 89.50)	(101.01, 126.55, 64.60, 576.30)
Nonlinear	(2.37, 1.18, 2.22, 5.69)	(0.04, 0.02, 0.04, 0.07)

Table 5. Results from 100 trajectory estimation runs for a single trajectory with additive Gaussian noise.

In our third study we utilized the data acquired from our volunteer as described in section 3.1. The 3D points acquired with the tracking system were positioned inside the viewing volume of the CBCT system, and projected using the system's projection matrices. The resulting 2D points were used to estimate the linear trajectory. In this case there is no known gold standard and evaluation was performed by comparing the mean distances between the known 3D points and the estimated lines. With the nonlinear approach the mean distances were (0.85mm, 0.56mm, 0.39mm, 0.30mm, 0.24mm, 0.29mm, 0.24mm), and with the analytic approach the corresponding mean distances were (1.64mm, 1.98mm, 1.50mm, 0.97mm, 0.68mm, 0.99mm, 0.90mm). Figure 3 summarizes this study.

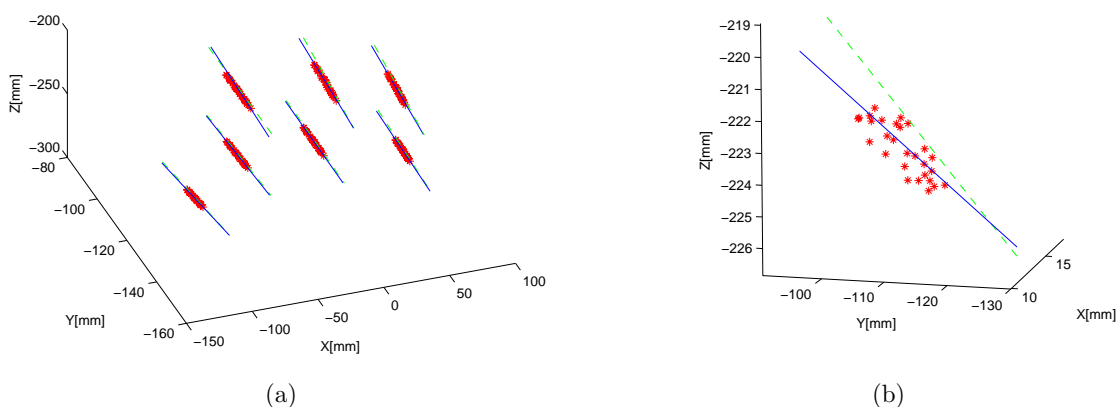
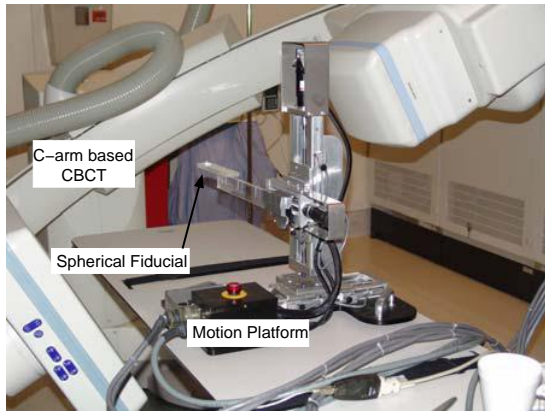


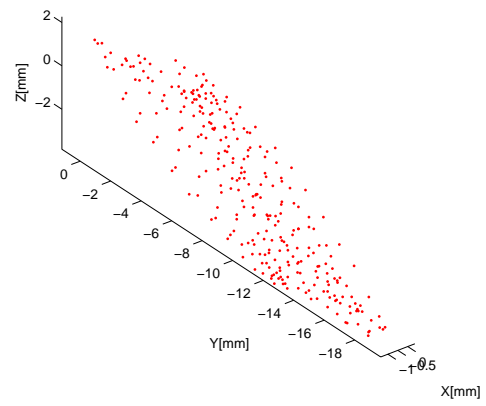
Figure 3. Trajectory reconstruction (a) all trajectories, (b) close up view of one trajectory. Red dots are the 3D coordinates as obtained from the Optotrak tracking system. Solid (blue) line was reconstructed using our nonlinear algorithm, dashed (green) line was reconstructed using the analytic method.

### 3.4 In-vitro evaluation

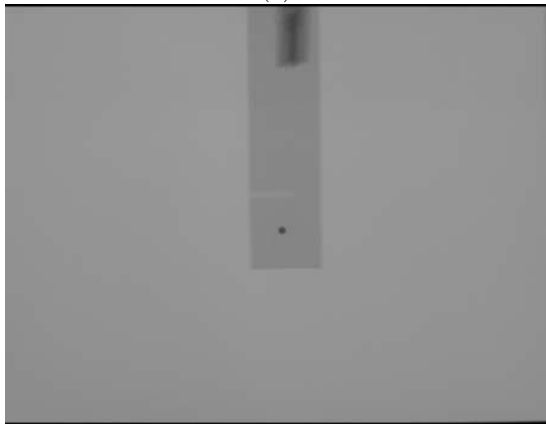
Finally, to evaluate our whole approach using a realistic in-vitro scenario we acquired CBCT scans of a fiducial mounted on a computer controlled motion platform that replicated the respiratory motion of our volunteer. Due to the limitations of the motion platform we had to resample the original 3D signal acquired at  $60Hz$  to a 3D signal at  $7.81Hz$  (a sample every  $128ms$ ). Given that we know the exact 3D motion we can generate a ground truth respiratory signal. This is done by performing PCA on the data and projecting it onto the major axis. The respiratory signal computed using our trajectory triangulation approach is then compared to this signal. The experimental setup the 3D data and sample X-ray images are shown in Figure 4.



(a)



(b)



(c)



(d)

Figure 4. In-vitro evaluation setup (a) motion platform (b) programmed 3D trajectory (c) and (d) sample X-ray images from two CBCT acquisition runs.

We observed that our respiratory signal is in phase with the ground truth signal, but suffers from inaccuracies in amplitude close to the anterior-posterior imaging setup where the primary direction of motion is perpendicular to the image plane. At this position (after half of the scanning time) the angle between the trajectory and the backprojected ray is small leading to errors in the estimation of the 3D fiducial location. Figure 5 shows the results from one of our data acquisition runs.

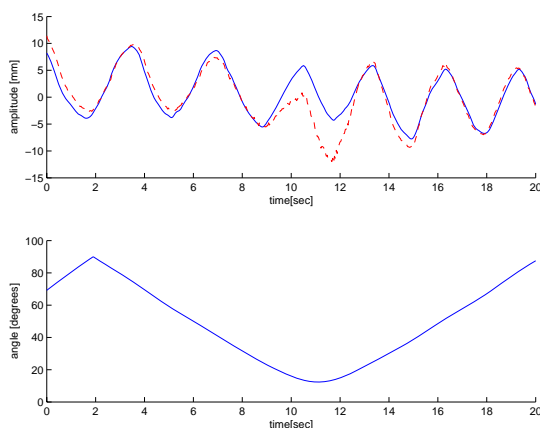


Figure 5. In-vitro evaluation results. Solid (blue) line is the ground truth respiratory signal generated from the known 3D points using PCA. Dashed (red) line is the respiratory signal generated via trajectory triangulation using the nonlinear algorithm. Results are accurate in phase but suffer from inaccuracies in amplitude when the angle between the trajectory and backprojected line is small.

#### 4. DISCUSSION AND CONCLUSIONS

We have presented a method for generating a respiratory signal that is implicitly synchronized with the acquisition of cone-beam CT. Unlike previous works our method is based on an explicit motion model and takes into account both the skin surface and C-arm motions. We have shown that our approach generates a respiratory signal that is in phase with a known signal but is inaccurate in amplitude when the angle between the C-arm’s viewing direction and main direction of motion is small. Thus the signal generated by our approach should be used for phase based binning and not amplitude based binning.

Matlab source code for the trajectory triangulation algorithms described in this paper is available at: <http://isiswiki.georgetown.edu/zivy/#software>.

#### ACKNOWLEDGMENTS

This work is part of a collaboration between the Chair for Computer Aided Medical Procedures (CAMP), Technical University of Munich, and the Computer Aided Interventions and Medical Robotics group, Georgetown University.

We would like to thank Emmanuel Wilson and David Lindisch for their help in conducting the experiments with the motion platform.

The work was funded by US Army grant W81XWH-04-1-0078. The content of this manuscript does not necessarily reflect the position or policy of the U.S. Government.

#### REFERENCES

1. T. M. Peters, “Image-guidance for surgical procedures,” *Phys. Med. Biol.* **51**(14), pp. R505–R540, 2006.
2. D. J. Hawkes, D. Barratt, J. Blackall, C. Chan, P. Edwards, K. Rhode, G. P. Penney, J. McClelland, and D. L. G. Hill, “Tissue deformation and shape models in image-guided interventions: a discussion paper,” *Medical Image Analysis* **9**(2), pp. 163–175, 2005.

3. F. Banovac, J. Tang, S. Xu, D. Lindisch, H. Y. Chung, E. B. Levy, T. Chang, M. F. McCullough, Z. Yaniv, B. J. Wood, and K. Cleary, "Precision targeting of liver lesions using a novel electromagnetic navigation device in physiologic phantom and swine," *Med. Phys.* **32**(8), pp. 2698–2705, 2005.
4. S. S. Vedam, P. J. Keall, V. R. Kini, H. Mostafavi, H. P. Shukla, and R. Mohan, "Acquiring a four-dimensional computed tomography dataset using an external respiratory signal," *Phys. Med. Biol.* **48**(1), pp. 45–62, 2003.
5. L. Boucher, S. Rodrigue, R. Lecomte, and F. Bénard, "Respiratory gating for 3-dimensional PET of the thorax: Feasibility and initial results," *Journal of Nuclear Medicine* **45**(2), pp. 214–219, 2004.
6. W. Kalender *et al.*, "Measurement of pulmonary parenchymal attenuation: use of spirometric gating with quantitative CT," *Radiology* **175**(1), pp. 265–268, 1990.
7. S. K. Carlson *et al.*, "Intermittent-mode CT fluoroscopy-guided biopsy of the lung or upper abdomen with breath-hold monitoring and feedback: System development and feasibility," *Radiology* **229**(3), pp. 906–912, 2003.
8. S. A. Nehmeh *et al.*, "Quantitation of respiratory motion during 4D-PET/CT acquisition," *Med. Phys.* **31**(6), pp. 1333–1338, 2004.
9. T. Pan, T.-Y. Lee, E. Rietzel, and G. T. Y. Chen, "4D-CT imaging of a volume influenced by respiratory motion on multi-slice CT," *Med. Phys.* **31**(2), pp. 333–340, 2004.
10. S. Wiesner and Z. Yaniv, "Monitoring patient respiration using a single optical camera," in *Annual International Conference of the IEEE EMBS*, pp. 2740–2743, 2007.
11. R. D. Beach, H. Depold, G. Boening, P. P. Bruyant, B. Feng, H. C. Gifford, M. A. Gennert, S. Nadella, and M. A. King, "An adaptive approach to decomposing patient-motion tracking data acquired during cardiac SPECT imaging," **54**(1), pp. 130–139, 2007.
12. M. A. Gennert, J. K. Ho, A. C. Quina, J. H. Wang, P. P. Bruyant, and M. A. King, "Feasibility of tracking patient respiration during cardiac SPECT imaging using stereo optical cameras," in *Nuclear Science Symposium*, **5**, pp. 3170–3172, 2003.
13. T. Li, L. Xing, P. Munro, C. McGuinness, M. Chao, Y. Yang, B. Loo, and A. Koong, "Four-dimensional cone-beam computed tomography using an on-board imager," *Med. Phys.* **33**(10), pp. 3825–3833, 2006.
14. S. Rit, D. Sarrut, and C. Ginestet, "Respiratory signal extraction for 4D CT imaging of the thorax from cone-beam CT projections," in *Medical Image Computing and Computer-Assisted Intervention*, pp. 556–563, 2005.
15. L. Zijp, J. J. Sonke, and M. V. Herk, "Extraction of the respiratory signal from sequential thorax cone-beam x-ray images," in *International Conference on the Use of Computers in Radiation Therapy*, pp. 507–509, 2004.
16. M. Mitschke and N. Navab, "Recovering the X-ray projection geometry for three-dimensional tomographic reconstruction with additional sensors: Attached camera versus external navigation system," *Medical Image Analysis* **7**(1), pp. 65–78, 2003.
17. J. Canny, "A computational approach to edge detection," *IEEE Trans. Pattern Anal. Machine Intell.* **8**(6), pp. 679–714, 1986.
18. M. A. Fischler and R. C. Bolles, "Random sample consensus: a paradigm for model fitting with applications to image analysis and automated cartography," *Commun. ACM* **24**(6), pp. 381–395, 1981.
19. W. Gander, G. H. Golub, and R. Strebler, "Least-squares fitting of circles and ellipses," *BIT* **34**(4), pp. 558–578, 1994.
20. S. Avidan and A. Shashua, "Trajectory triangulation: 3D reconstruction of moving points from a monocular image sequence," *IEEE Trans. Pattern Anal. Machine Intell.* **22**(4), pp. 348–357, 2000.
21. A. Bartoli and P. Sturm, "The 3D line motion matrix and alignment of line reconstructions," *International Journal of Computer Vision* **57**(3), pp. 159–178, 2004.
22. K. Wiesent, K. Barth, N. Navab, P. Durlak, T. Brunner, O. Schütz, and W. Seissler, "Enhanced 3D-reconstruction algorithms for C-arm based interventional procedures," *IEEE Trans. Med. Imag.* **19**(5), pp. 391–403, 2000.
23. R. Lin, E. Wilson, J. Tang, D. Stoianovici, and K. Cleary, "A computer-controlled pump and realistic anthropomorphic respiratory phantom for validating image-guided systems," in *SPIE Medical Imaging: Visualization and Image-Guided Procedures*, 2007.